

The Signature of Strong High-Redshift Radio Backgrounds on the Cosmic Dawn 21-cm Bispectrum

Sudipta Sikder,¹[★] Rajesh Mondal,² Rennan Barkana¹ and Anastasia Fialkov^{3,4}

¹*School of Physics and Astronomy, Tel-Aviv University, Tel-Aviv, 69978, Israel*

²*Department of Physics, National Institute of Technology Calicut, Calicut 673601, Kerala, India*

³*Institute of Astronomy, University of Cambridge, Madingley Road, Cambridge, CB3 0HA, UK*

⁴*Kavli Institute for Cosmology, Madingley Road, Cambridge, CB3 0HA, UK*

arXiv:2602.13445v1 [astro-ph.CO] 13 Feb 2026

Accepted XXX. Received YYY; in original form ZZZ

ABSTRACT

Measurements from the Absolute Radiometer for Cosmology, Astrophysics, and Diffuse Emission 2 (ARCADE-2) reveal a strong radio background in the GHz frequency range. Since the cosmological 21-cm signal is measured relative to the background radiation temperature, the presence of a radio excess can significantly alter its characteristics. Previous studies have explored the impact of an inhomogeneous radio background on the global 21-cm signal and 21-cm power spectrum. This non-uniform radio background is also expected to introduce substantial non-Gaussianity. In this work, using the bispectrum, we analyze the non-Gaussianity in the 21-cm signal in the presence of an excess galactic radio background and investigate how line-of-sight radio fluctuations from early galaxies influence its nature. We find that even a moderate enhancement in radio efficiency in early galaxies significantly affects the small-scale 21-cm bispectrum. Furthermore, the delayed heating transition caused by a galactic radio background shifts the sign change in the squeezed-limit bispectrum to lower redshifts ($z \sim 11$), providing a potential observational signature for distinguishing different radio background models. These results demonstrate that the 21-cm bispectrum, particularly in the squeezed limit, is highly sensitive to radio background fluctuations, making it a powerful tool for probing high-redshift radio-loud sources and the physics of the early cosmic epoch.

Key words: methods: numerical – methods: statistical – dark ages, reionization, first stars – cosmology: observations – cosmology: theory

1 INTRODUCTION

The Universe expanded and cooled after the Big Bang. This cooling led to the formation of neutral hydrogen atoms, as electrons and protons combined. Radiation and matter then decoupled, which marked the end of the Epoch of Recombination. The universe remained dark for a time after this. However, the first luminous structures eventually formed, during a phase known as the Cosmic Dawn (CD). These first luminous sources emitted ionizing radiation, which gradually ionized the neutral hydrogen in the intergalactic medium (IGM). This period is therefore known as the Epoch of Reionization (EoR). The limited number of observations has hindered our understanding of the CD-EoR. However, a considerable international observational effort is underway to learn more about this important period in the history of the universe.

The redshifted 21-cm signal is a powerful probe of astrophysical and cosmological information during the CD-EoR. This signal arises due to the hyperfine transition of the electron-proton system from parallel to anti-parallel spin in the ground state of neutral hydrogen (HI). Several low-frequency radio interferometers, such as GMRT¹ (Swarup et al. 1991), LOFAR² (van Haarlem et al. 2013),

MWA³ (Tingay et al. 2013), and HERA⁴ (DeBoer et al. 2017), have been dedicated to detecting the fluctuations in the 21-cm signal from the EoR. However, the signal is very weak, being approximately 4 to 5 orders of magnitude smaller than the foreground emission (see e.g., Ali et al. 2008). This has posed great challenges to these observational efforts. Despite these challenges, the first-generation radio interferometers have successfully put significant upper limits on the expected fluctuations in the EoR 21-cm signal (Barry et al. 2019; Li et al. 2019; Mertens et al. 2020; Trott et al. 2020; Abdurashidova et al. 2022b). These upper limits have placed constraints on the properties of early galaxies and the IGM during the EoR (see e.g., Mondal et al. 2020; Ghara et al. 2020; Greig et al. 2021; Abdurashidova et al. 2022a). The next generation telescope, the SKA⁵ (Koopmans et al. 2015), is expected to be much more sensitive than its predecessors. Therefore it is likely to be able to detect the fluctuations in the 21-cm signal from the CD-EoR. The detection of the 21-cm signal from the EoR would be a major breakthrough in astronomy. It would allow us to study the formation of the first stars and galaxies, and to learn more about the evolution of the universe at this early epoch.

The CD-EoR 21-cm signal is highly non-Gaussian due to the un-

[★] E-mail: sudiptas@mail.tau.ac.il

¹ <http://www.gmrt.ncra.tifr.res.in>

² <http://www.lofar.org/>

³ <http://www.mwatelescope.org/>

⁴ <https://reionization.org/>

⁵ <http://www.skatelescope.org/>

derlying non-linear matter density field, non-uniform Ly- α coupling, non-uniform heating of HI gas, and the formation of ionized regions that should appear as holes in the 21-cm signal (see e.g., Bharadwaj & Pandey 2005; Mondal et al. 2015; Kamran et al. 2022). One-point statistics such as the probability distribution function (pdf) (Ciardi & Madau 2003; Mellema et al. 2006; Ichikawa et al. 2010), skewness and kurtosis (Wyithe & Morales 2007; Harker et al. 2009; Watkinson & Pritchard 2014, 2015; Shimabukuro et al. 2015; Kubota et al. 2016; Kittiwisit et al. 2017) can be used to quantify this non-Gaussianity, but they do not describe its scale dependence.

The spherically averaged power spectrum (SAPS) measures the variance of the 21-cm signal at different length scales. It quantifies the amplitudes of the fluctuations in the signal at different wavenumbers k . The SAPS fully describes the statistical properties of a field that consists of Gaussian random fluctuations (see e.g., Mondal et al. 2016). However, due to the non-Gaussianity present in the CD-EoR signal, the SAPS does not fully quantify the statistical information. For this, we need higher-order statistics, such as the bispectrum (see e.g., Peebles 1980).

The bispectrum is the Fourier transform of the three-point correlation function. It depends on three \mathbf{k} vectors that form a closed triangle. Bharadwaj & Ali (2005) first studied the non-Gaussianity of the EoR 21-cm signal using an analytical model consisting of spherical ionized regions. They showed that the bispectrum can be both positive and negative. Watkinson et al. (2017) and Majumdar et al. (2018) independently confirmed these findings using two different bispectrum estimators.

The spherically averaged bispectrum (SABS) can be characterized by the size (scale factor) and the shape of the triangles (Bharadwaj et al. 2020; see Section 4.1 for more details). Using this framework, many studies (see e.g., Majumdar et al. 2020; Kamran et al. 2022) have shown that the 21-cm CD-EoR SABS can be used to distinguish between different sources of non-Gaussianity in the signal, and to learn more about the physical processes that are responsible for the formation of the first stars and galaxies. Notably, Mondal et al. (2021) demonstrated that the squeezed limit bispectrum, among all possible triangle shapes, offers the highest signal-to-noise ratio for detection with the SKA, making it a focal point for observational efforts. However, to fully capture the diversity of non-Gaussian signatures and their physical implications, it is valuable to explore a range of triangle configurations beyond just the squeezed limit. Therefore, while this work emphasizes the squeezed limit bispectrum due to its detectability, it also investigates other triangle configurations to provide a more complete picture of the statistical properties of the 21-cm signal.

The EDGES experiment has claimed to detect a global 21-cm signal (Bowman et al. 2018) in the frequency range 50 to 100 MHz that is significantly stronger than predicted from standard astrophysical assumptions. This anomalous absorption trough is centered at redshift 17 (corresponding to a frequency of 78 MHz) and has an amplitude of $T_{21} = -500^{+200}_{-500}$ mK. Various non-standard theoretical models and new physics have been proposed to explain this signal. Although the SARAS3 experiment has disputed the EDGES signal at 95% confidence (Singh et al. 2022), the debate over the origin of this anomalous absorption trough is ongoing. Future experiments may be able to resolve the issue. Therefore, in this paper we consider the possibility that the EDGES signal could turn out to be correct.

The ARCADE2 (Fixsen et al. 2011; Seiffert et al. 2011) experiment made a noteworthy discovery of excess radio background over the cosmic microwave background (CMB) at low frequencies. This excess was subsequently corroborated by the LWA1 (Dowell & Taylor 2018) experiment in the frequency range of 40-80 MHz. The origin of

this radio excess is still unclear, but it could potentially be attributed to extragalactic sources. However, the exact fraction of this observed excess that stems from galactic sources compared to extragalactic sources remains unclear (e.g., Subrahmanyan & Cowsik 2013). Various models of the excess radio background have been proposed, and their effects on the 21-cm signal have been studied in recent years. Fialkov & Barkana (2019) explored the effect of a uniform external radio background, not directly related to any astrophysical sources, on the 21-cm signal, focusing on the context of the EDGES low-band observation. In this work, we examine whether such a background introduces additional non-Gaussianity by computing the bispectrum within this model. Also, inhomogeneous galactic radio background models have been proposed by Reis et al. (2020); Sikder et al. (2023). These models predict significant enhancement of the 21-cm power spectrum from the CD-EoR. This non-uniform radio background is also expected to introduce significant non-Gaussianity in the 21-cm signal. However, the impact of this non-uniform excess radio background originating from high-redshift galaxies (Condon et al. 2012; Ewall-Wice et al. 2018; Mirocha & Furlanetto 2019; Mebane et al. 2020) on the 21-cm bispectrum has not yet been explored. In this study, we investigate the 21-cm bispectrum within the context of an excess galactic radio background. We also examine how radio fluctuations along the line of sight from these galaxies impact the 21-cm bispectrum.

The paper is structured as follows: We briefly describe our semi-numerical cosmic dawn simulation in section 2. In section 3, we summarize the non-standard excess radio models and their implications for the 21-cm power spectrum and global signal. We briefly present the theoretical background and algorithm that has been used to generate the 21-cm bispectrum from a simulated 21-cm signal for all possible triangle configurations in section 4. We present our main results in section 5. Finally, in section 6, we conclude the paper with a summary. Throughout this study, we use the Λ CDM cosmology with cosmological parameters from the Planck Collaboration et al. (2016).

2 SEMI-NUMERICAL SIMULATION

To generate the 21-cm signal over a wide range of redshifts, we use our 21-cm Semi-numerical Predictions Across Cosmic Epochs (21cmSPACE) simulation code (see e.g., Visbal et al. 2012; Fialkov & Barkana 2014; Cohen et al. 2017; Fialkov & Barkana 2019). The outputs of the simulation are 21-cm brightness temperature cubes in a $[384 \text{ Mpc}]^3$ comoving cosmological volume with a resolution of 3 comoving Mpc over a wide range of redshifts (6 to 35). We calculate the global signal, power spectrum, bispectrum, etc. using those simulation boxes at each redshift.

We use the publicly available code CAMB⁶ (Lewis et al. 2000) to calculate the power spectra of initial density fields. We then obtain Gaussian random realizations of density fluctuations and the relative velocity between dark matter and baryon (Tseliakhovich & Hirata 2010). The population of collapsed dark matter halos inside each cell is modeled analytically following a hybrid prescription by Barkana & Loeb (2004), which is based on the Press-Schechter formalism (Press & Schechter 1974) and the Sheth-Tormen mass function (Sheth & Tormen 1999). This approach has been slightly modified to account for the effect of the relative baryon-dark matter velocity (v_{bc}) on the

⁶ <https://camb.info/>

number of halos in each pixel, following the framework of Fialkov et al. (2012) (see also, Tseliakhovich et al. 2011).

We assume that galaxies only form within halos where the circular velocity exceeds a specific threshold, denoted as V_c . This threshold is a proxy for the minimum mass of the star-forming halos, which is required for radiative cooling of the infalling gas. In this study, we consider star formation set by atomic cooling by choosing $V_c = 16.5 \text{ km s}^{-1}$ which corresponds to $M_{\min} \approx 3 \times 10^7 M_\odot$ at $z = 20$. Another important parameter is the star formation efficiency⁷, f_* , which quantifies the fractional gas mass in star-forming halos that is converted into stellar mass. Since the detailed mechanisms of star formation are highly unconstrained at high redshift due to the dearth of direct observations, f_* is treated as one of the free parameters in the simulation. We fixed f_* to be 0.1 for the results presented in this work. The simulation also takes into account the effects of the dark matter-baryons relative velocity, Lyman-Werner feedback on molecular cooling halos (Haiman et al. 1997; Fialkov et al. 2013), and photoheating feedback (Rees 1986; Sobacchi & Mesinger 2013; Cohen et al. 2016) on the suppression of star formation.

The formation of a population of galaxies is followed by the computation of the radiation fields emitted by these galaxies. The primary radiation fields that have a significant impact on the 21-cm signal are Ly- α radiation, X-ray radiation, and ionizing radiation. Ly- α photons are responsible for the Wouthuysen-Field coupling and these photons also heat up the IGM. To determine the intensity of the Ly- α radiation field, we assume that galaxies consist of population II stars and that for a given galaxy, Ly- α radiation is proportional to its star formation rate (SFR). The X-ray luminosity is also assumed to scale with the SFR as follows (Fialkov et al. 2014),

$$\frac{L_X}{\text{SFR}} = 3 \times 10^{40} f_X \text{ erg s}^{-1} M_\odot^{-1} \text{ yr}, \quad (1)$$

where the additional normalization factor, f_X is the X-ray radiation efficiency of the sources. $f_X = 1$ corresponds to the typical observed X-ray luminosity of low-metallicity galaxies at low redshifts (see e.g., Grimm et al. 2003; Gilfanov et al. 2004; Mineo et al. 2012; Fragos et al. 2013; Fialkov et al. 2014; Pacucci et al. 2014). We choose $f_X = 1$ for all the simulation runs shown in this work. In addition to the X-ray luminosity, the shape of the X-ray spectral energy density (SED) also affects the 21-cm signal. We assume a power law shape for the X-ray SED, where the slope (α) and the low energy cutoff (E_{\min}) determine the shape of the power law. Both α and E_{\min} are two free parameters in our simulation. For this work, we set $\alpha = 1.5$ and $E_{\min} = 1 \text{ keV}$ for the X-ray SED.

The 21-cm signal during reionization is primarily governed by x_{HI} fluctuations, rather than by other factors such as heating, Lyman-alpha coupling, and density fluctuations. The process of reionization is modeled using the excursion set formalism, as described by Furlanetto et al. (2004). In this formalism, a specific region is considered to be ionized if the fraction of collapsed matter surpasses a threshold of ζ^{-1} , where ζ represents the overall efficiency of ionizing sources. The course of reionization also depends on the maximum distance traveled by ionizing photons, i.e., the mean free path of ionizing photons, R_{mfp} , another free parameter in the simulation (see e.g., Greig & Mesinger 2015). R_{mfp} represents an effective upper limit for the size of ionization bubbles formed during the EoR. We used a fixed value of $\zeta = 30$ and $R_{\text{mfp}} = 30 \text{ Mpc}$ (comoving) for all the

⁷ The latest 21cmSPACE supports two populations of stars with a realistic Pop III - Pop II transition (Gessey-Jones et al. 2022). Throughout this work, we only consider the Pop II star formation prescription from Visbal et al. (2012) and Fialkov et al. (2013).

cases analyzed in this study. Note that the reionization model in this simulation has some limitations compared to simulations that only focus on the EoR (see e.g., Iliev et al. 2007; Mondal et al. 2017). However, our main concern is to study the 21-cm bispectrum during the cosmic dawn (CD), so these limitations are not a major drawback for our work.

3 NON-STANDARD RADIO BACKGROUND MODELS

The 21-cm brightness temperature, T_{21} , is proportional to the difference between the spin temperature, T_S , of neutral hydrogen and the background radiation temperature, T_{rad} . From the solution of the radiative transfer equation in an expanding universe, T_{21} can be written as

$$T_{21} = \frac{T_S - T_{\text{rad}}}{1 + z} (1 - e^{-\tau_{21}}). \quad (2)$$

In the standard astrophysical scenario, we assume the background radiation to be the CMB at redshift z , i.e., $T_{\text{rad}} = T_{\text{CMB}} = 2.725(1 + z) \text{ K}$. However, in the case of a non-standard excess radio model, the background radiation temperature can be written as

$$T_{\text{rad}} = T_{\text{Radio}} + T_{\text{CMB}}, \quad (3)$$

where T_{Radio} is the brightness temperature of the radio excess. The mathematical equation for T_{Radio} pertains exclusively to the modeling of the excess radio background. In simulations with an excess radio background, the astrophysical parameters (f_* , V_c , f_X , α , E_{\min} , ζ , R_{mfp}) retain the same values and roles as in the standard CMB background case (Section 2). Recent studies (Acharya et al. 2023; Cyr et al. 2024) suggest that soft photon heating can modify the shape and amplitude of the 21-cm signal in the presence of a radio background during the cosmic dawn. However, this effect is not considered in the present work. Below, we describe the non-standard excess radio models considered in this study.

3.1 Exotic uniform radio background

A simple, homogeneous excess radio background that might not be directly related to astrophysical sources was proposed by Feng & Holder (2018). This background could arise from exotic processes such as dark matter decay (see, e.g., Fraser et al. 2018; Pospelov et al. 2018) and super conducting cosmic strings (see e.g., Brandenberger et al. 2019). Therefore, its intensity is not dependent on the star formation history. Fialkov & Barkana (2019) first explored its impact on 21-cm fluctuations. The brightness temperature of this exotic uniform radio excess at the 21-cm rest frame frequency at z can be written as

$$T_{\text{Radio}} = 2.725(1 + z) A_r \left[\frac{\nu_{\text{obs}}}{78 \text{ MHz}} \right]^\beta \text{ K}, \quad (4)$$

where 2.725 K is the present day CMB temperature. Here β is the spectral index of the synchrotron spectrum, which is set to -2.6 to match the observed spectrum (Fixsen et al. 2011; Seiffert et al. 2011; Dowell & Taylor 2018) of the extragalactic radio background, ν_{obs} is the observed frequency and A_r is the amplitude of the radio background relative to the CMB at the EDGES peak frequency of 78 MHz. To investigate its effect on the 21-cm bispectrum, we set the amplitude A_r , which regulates the strength of the radio background, at 0.0945, a value chosen to ensure that the global signal trough in our excess radio model deviates only modestly, by less than 15%, from that of the standard astrophysical scenario. By keeping the global signal close to the standard scenario, we can test how even

a modest excess can impact higher-order statistics, particularly the 21-cm bispectrum.

3.2 Radio fluctuations from high redshift galaxies

In contrast to the phenomenological description of the excess radio background with a synchrotron spectrum, high redshift radio-loud sources such as star-forming galaxies or Active Galactic Nuclei (AGN) could produce an excess radio background over the CMB. The modeling of this astrophysical radio excess and its impact on the global 21-cm signal has been investigated by [Ewall-Wice et al. \(2018\)](#) and [Mirocha & Furlanetto \(2019\)](#). [Reis et al. \(2020\)](#) first incorporated this non-uniform excess radio background from high redshift galaxies into a semi-numerical simulation code for cosmic dawn, and explored the effect on the 21-cm power spectrum. In this galactic radio model, the radio luminosity of galaxies is assumed to be proportional to the SFR, as (based on the empirical relation of [Gürkan et al. 2018](#))

$$L_{\text{Radio}}(\nu, z) = f_{\text{Radio}} 10^{22} \left(\frac{\nu}{150 \text{ MHz}} \right)^{-\alpha_{\text{Radio}}} \left(\frac{\text{SFR}}{M_{\odot} \text{ yr}^{-1}} \right) \frac{\text{W}}{\text{Hz}}, \quad (5)$$

where α_{Radio} is the spectral index in the radio band which is set to 0.7 as in [Mirocha & Furlanetto \(2019\)](#) and [Gürkan et al. \(2018\)](#). f_{Radio} is the normalization of the radio emissivity so that for present day star-forming galaxies, the value of f_{Radio} is 1. In the case of a simplified model with the approximation of an isotropic galactic radio background ([Reis et al. 2020](#)), the radio background brightness temperature at 21-cm frequency at redshift z is determined by adding up the contribution from all the galaxies within the past light-cone:

$$T_{\text{Radio}}(\nu_{21}, z) = \frac{\lambda_{21}^2}{2k_{\text{B}}} \frac{c(1+z)^3}{4\pi} \times \int \epsilon_{\text{Radio}} \left(\nu_{21} \frac{1+z_{\text{em}}}{1+z}, z_{\text{em}} \right) (1+z_{\text{em}})^{-1} H(z_{\text{em}})^{-1} dz_{\text{em}}, \quad (6)$$

where z_{em} is the redshift of photon emission, and the comoving radio emissivity ϵ_{Radio} is the radio luminosity per unit frequency per unit comoving volume averaged over radial shells in this spherical integral. The computation of T_{Radio} follows a similar approach to that of the Ly- α and X-ray radiation fields, assuming an isotropically averaged intensity at each pixel in the simulation box. However, the assumption of isotropy of the radio background is only approximate. In the next section, we present a more precise and realistic model of the excess radio background from galaxies at high redshift.

3.3 LoS radio fluctuation model

Since the 21-cm absorption occurs along the line-of-sight (LoS), the radiative transfer calculation along the line of sight depends solely on the radio intensity from sources located behind the hydrogen cloud, along the LoS. However, the isotropically averaged radio intensity is the relevant quantity for physical effects such as the calculation of Lyman- α coupling coefficients. [Sikder et al. \(2023\)](#) illustrated the effect of these LoS radio fluctuations on the 21-cm signal. The brightness temperature of the radio background from sources that contribute along the LoS ($T_{\text{Radio,LoS}}$) is calculated similarly to T_{Radio} . However, unlike T_{Radio} , where a source emitting at z_{em} contributes a spherical shell around the source, $T_{\text{Radio,los}}$ receives contributions from the same source only along a single direction, i.e., the LoS direction. In contrast to previous non-standard cases mentioned above (eqs. 2, 4 and 5), the 21-cm brightness temperature for this case can

be written as (for details, see [Sikder et al. 2023](#))

$$T_{21} = \frac{T_S - (T_{\text{Radio,LoS}} + T_{\text{CMB}})}{1 + z} (1 - e^{-\tau_{21}}). \quad (7)$$

For both isotropic and line-of-sight considerations in non-uniform galactic radio background models, the parameter f_{Radio} quantifies the strength of the radio background. In this work, unless otherwise specified, we adopt $f_{\text{Radio}} = 60$ for the examples presented. This moderate value is chosen so that the global signal trough in this excess radio model lies within 15% of that of the standard CMB-only scenario. This choice allows us to investigate how a mild excess background from early galaxies influences 21-cm fluctuations, particularly the 21-cm bispectrum. We also investigate an $f_{\text{Radio}} = 3000$ model in order to see the impact of a high radio source model; this is roughly the highest value allowed for a galaxy population at $z \sim 20$ by clustering of the radio background, which sets the strongest current observational constraint on such models ([Sikder et al. 2024](#)). For convenience, we list in Table 1 the parameters along with their values, including those in the excess radio models.

We emphasize that the LoS radio fluctuation model should be considered the main, most interesting model for comparison with the standard case (CMB only, i.e., no radio background). In comparison, the exotic radio background model is an ad-hoc model, while the others have an astrophysical motivation as they place the radio emission in galaxies (though with an unusually enhanced amplitude of radio emission). The radio fluctuation model with isotropy is only an approximate model that removes some of the realism of the LoS model and thus allows us to isolate the effect of the LoS anisotropy on the results. In summary, the LoS galactic radio fluctuation model is both astrophysically motivated and accurately calculated.

4 21-CM BISPECTRUM

The bispectrum is a statistical measure of three-point correlations of a field in Fourier space. Mathematically, the bispectrum of the 21-cm brightness temperature field can be written as

$$\langle \Delta(\mathbf{k}_1) \Delta(\mathbf{k}_2) \Delta(\mathbf{k}_3) \rangle = B(\mathbf{k}_1, \mathbf{k}_2, \mathbf{k}_3) V \delta_D(\mathbf{k}_1 + \mathbf{k}_2 + \mathbf{k}_3), \quad (8)$$

where $\Delta(\mathbf{k})$ is the Fourier transform of the brightness temperature fluctuations, V is the comoving volume under consideration, and the angular brackets denote an ensemble average over different realizations of the field. The Dirac delta function δ_D , which equals 0 unless $\mathbf{k}_1 + \mathbf{k}_2 + \mathbf{k}_3 = 0$, ensures that the Fourier modes form a closed triangle.

4.1 Unique triangle configurations in Fourier space

We use the parameterization from [Bharadwaj et al. \(2020\)](#) to identify all possible unique triangle configurations in Fourier space. This formalism characterizes the size and shape of a triangle by designating the largest side as \mathbf{k}_1 and the second-largest side as \mathbf{k}_2 which implies $k_1 \geq k_2 \geq k_3$, where k represents the amplitude of the vector \mathbf{k} . The following two parameters relate k_1 and k_2 in a way that quantifies the size and shape of the triangle:

$$\text{Size parameter: } n = \frac{k_2}{k_1}, \quad (9)$$

$$\text{Shape parameter: } \cos \theta = -\frac{\mathbf{k}_1 \cdot \mathbf{k}_2}{k_1 k_2}, \quad (10)$$

where θ is the angle between $-\mathbf{k}_1$ and \mathbf{k}_2 . The value of n is restricted to the range $0.5 \leq n \leq 1$, and $\cos \theta$ is limited by $n \cos \theta \geq 0.5$.

Parameter	Values	Description
f_\star	0.1	Star formation efficiency
V_c	16.5 km s ⁻¹	Minimum circular velocity
f_X	1	X-ray production efficiency
α	1.5	Slope of X-ray SED
E_{\min}	1 keV	X-ray SED low energy cutoff
ζ	30	the overall efficiency of ionizing sources
R_{mfp}	30 Mpc	Mean free path for ionizing photons
f_{Radio}	60 or 3000	Radio production efficiency (radio from early galaxies)
A_r	0.0945	Amplitude of uniform radio background (radio from exotic processes)

Table 1. The parameters and their values used in this work. The model labeled “Radio fluctuations” assumes the isotropic approximation, and always has moderate efficiency ($f_{\text{Radio}} = 60$). Once we add the LoS effect, we assume moderate efficiency by default, unless we indicate high efficiency ($f_{\text{Radio}} = 3000$).

It is common to study specific triangle configurations to interpret the bispectrum, such as the equilateral triangle, isosceles triangle, linear triangle, and squeezed triangle. Each of these configurations quantifies distinct non-Gaussian properties of the field.

4.2 The Bispectrum estimator

The spherically averaged binned bispectrum estimator for the i -th bin is defined as

$$\hat{B}_i(k_1, n, \cos \theta) \equiv \hat{B}_i(k_1, k_2, k_3) = \frac{1}{N_t V} \sum_t \Delta(\mathbf{k}_1) \Delta(\mathbf{k}_2) \Delta(\mathbf{k}_3), \quad (11)$$

where t indexes triangles in the i -th bin and \sum_t is over the number N_t of closed triangles within the i -th bin. The bins are three-dimensional (3D) voxels of volume $[\Delta k_1 \Delta k_2 \Delta k_3]$, which we map to the $(k_1, n, \cos \theta)$ space using eqs. (9) and (10). The ensemble average of the estimator is the bin-averaged spherically averaged bispectrum (SABS): $\langle \hat{B}(k_1, n, \cos \theta) \rangle = \bar{B}(k_1, n, \cos \theta)$.

The bispectrum is a measure of the statistical dependence of three wave vectors. To calculate the bispectrum, we need to include the condition $\mathbf{k}_1 + \mathbf{k}_2 = -\mathbf{k}_3$. The direct estimation method is the most accurate method for calculating the bispectrum, but it is also the most computationally expensive. A conventional direct estimation method requires six nested for loops, three of which are used to find \mathbf{k}_1 and the other three to find \mathbf{k}_2 . This results in an order of N_G^6 operations, where N_G is the number of grid points along each direction.

To reduce computational cost, Mondal et al. (2021) proposed some optimization and parallelization methods. We use their publicly available bispectrum estimation code DviSukta⁸. This code employs the direct estimation method and has been optimized for speed and efficiency. Here we provide a brief summary of the algorithm used in DviSukta. For a more detailed description, the reader is referred to Section 2.2 of Mondal et al. (2021).

The algorithm begins by partitioning the Fourier space into a set of non-overlapping cells. The bispectrum is then calculated for each cell using the direct estimation method. The code first searches for all possible \mathbf{k}_1 and bins them using equally spaced spherical logarithmic binning. Inside the \mathbf{k}_1 loop, the code searches for all possible \mathbf{k}_2 using eq. 9 and partial use of eq. 10. The bispectrum values from the $(\mathbf{k}_2, \mathbf{k}_3)$ space are then mapped to the $(n, \cos \theta)$ space and binned using equally spaced linear bins. The results from the individual cells are then combined and the bin averaging is performed to produce $\bar{B}(k_1, n, \cos \theta)$.

⁸ <https://github.com/rajeshmondal18/DviSukta>

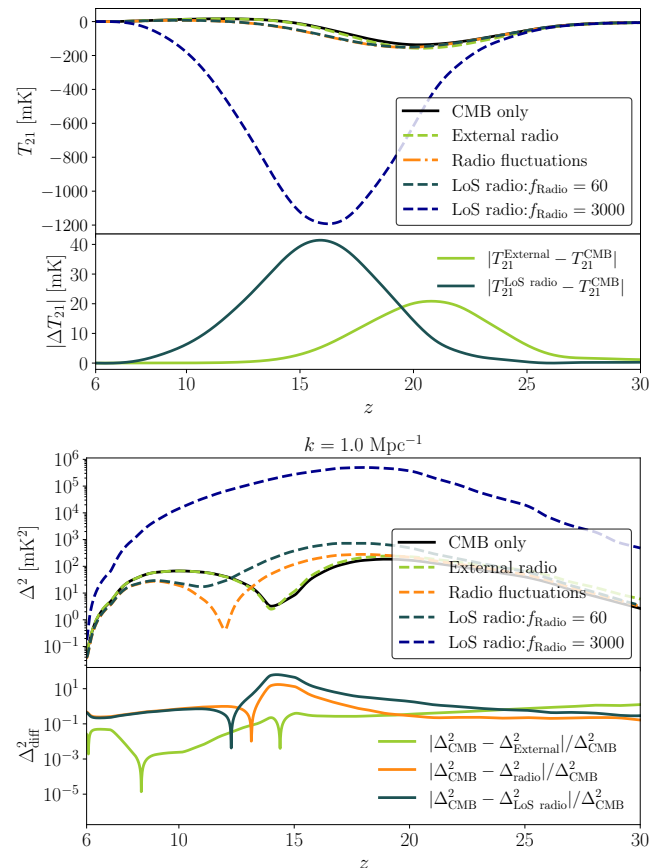


Figure 1. Top panel: Global signal as a function of redshift for the astrophysical models considered in this work. We also show the absolute differences in the global signal for the external (green solid) and moderate LoS radio fluctuation model (teal solid) compared to the standard astrophysical model. **Bottom panel:** The 21-cm power spectrum at $k = 1.0 \text{ Mpc}^{-1}$ as a function of redshift for the five different models. The relative differences of three excess radio models with respect to the standard astrophysical model are also shown.

To show our results, we use the scale-independent spherically averaged bispectrum, which is defined as

$$\Delta^3(k_1, n, \cos \theta) \equiv \frac{k_1^6 n^3 B(k_1, n, \cos \theta)}{(2\pi^2)^2}. \quad (12)$$

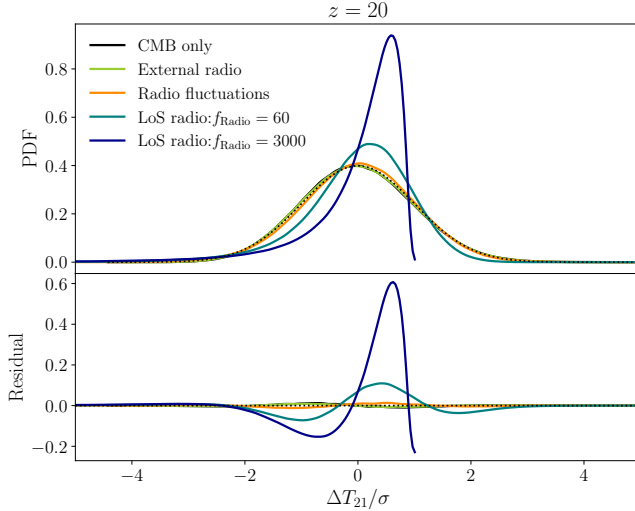


Figure 2. Top panel: Probability density functions (PDFs) of the 21-cm brightness temperature, measured relative to the mean temperature and divided by the standard deviation, for various models at $z = 20$: standard astrophysical model (black solid line), external radio background model (green solid line), isotropic galactic radio fluctuation model (orange solid line), and LoS galactic radio fluctuation models with $f_{\text{Radio}} = 60$ (teal solid line) or $f_{\text{Radio}} = 3000$ (blue solid line). Note that the PDFs are normalized to a total area of unity, and the standard deviation for these five cases is $\sigma = 15.47, 18.23, 18.73, 24.89$ and 611.0 mK, respectively. We also compare to a Gaussian PDF (black dotted curve), which has mean 0 and $\sigma = 1$ in these normalized units. **Bottom panel:** We show the difference between each PDF and the Gaussian PDF, for the various models. This quantifies one kind of non-Gaussianity in the 21-cm brightness temperature. Also shown for comparison is a zero difference (black dotted line).

5 RESULTS

5.1 The 21-cm global signal, power spectrum, and probability distribution function

We first examine the one-point and two-point statistics, namely the global signal and power spectrum, for the same set of astrophysical parameters (see Table 1), to get a baseline overview. This is helpful for understanding the next higher statistic, the bispectrum.

Figure 1 shows the all-sky-averaged global signal (top panel) and 21-cm power spectrum at $k = 1.0 \text{ Mpc}^{-1}$ (bottom panel) as a function of redshift for five different models. In the top panel, the maximum absorption for the expected signal from the standard astrophysical scenario (CMB only, black solid line) occurs with an amplitude of -136.9 mK at $z = 20.2$, corresponding to $\nu \sim 67$ MHz. We also consider three moderate excess radio models: uniform external radio excess, isotropic radio fluctuation, and a line-of-sight (LoS) radio fluctuation model, for which the maximum signal amplitudes are -157.4 (green dashed line), -152.3 (dark orange dot-dashed line) and -151.4 (teal dashed line) mK, occurring at $z = 20.3, 19.7$ and 19.7 , respectively. These models have moderate values of the radio production efficiency parameter, i.e., $f_{\text{Radio}} = 60$ for the galactic radio background models and $A_r = 0.0945$ for the radio background of the external model, such that the global signal minima of these excess radio models are within 15% of that of the standard astrophysical model (CMB-only case). This allows us to probe the 21-cm bispectrum signatures associated with moderate excess radio backgrounds, even when their global signals are not easily distinguished from the standard (no radio) case. Separately we also show the high

radio excess model ($f_{\text{Radio}} = 3000$, for the full galactic radio background model with the line-of-sight effect), which has an order of magnitude deeper trough.

In a separate frame within the top panel we show the absolute differences between the global signals ($T_{21}^{\text{External}}, T_{21}^{\text{LoS radio}}$) of two excess radio models and that of the CMB-only case (T_{21}^{CMB}). For the LoS galactic radio background model, the maximum absolute difference is ~ 40 mK, occurring at $z \sim 16$, while for the external radio model, the absolute difference peaks at $z \sim 20$ with an amplitude of ~ 20 mK. We do not show the absolute difference for two other models: the isotropic radio fluctuation model yields a global signal essentially identical to that of the LoS radio fluctuation model (due to the averaging that is inherent in the global signal); and for the high radio excess model, the difference with the other models is clear.

The bottom panel of Figure 1 displays the 21-cm power spectrum for the same set of models discussed earlier, highlighting the effects of various excess radio background scenarios. Compared to the standard astrophysical case, the two galactic radio models exhibit significant boosts in power. The line-of-sight (LoS) model achieves a maximum relative difference of a factor of ~ 63 at $z \sim 14$, while the isotropic model shows a more modest increase of ~ 17 . These differences reflect the amplified 21-cm signal driven by the spatially varying radio background, with the stronger effect of the LoS model resulting from the additional contribution to fluctuations of the directional dependence along the line of sight. In contrast, the uniform external radio background has a far less pronounced impact on the power spectrum, particularly at low redshifts. For instance, at $z = 15$, the relative difference due to the uniform radio background is only 0.39, rising to 0.73 at $z = 25$. The redshift dependence - where the effect of uniform radio excess weakens from $z = 25$ to $z = 15$ - reflects the fact that this smooth external background effectively declines with cosmic time. In contrast, the galactic radio backgrounds grow stronger over time, tracing the growth of galaxy formation.

To show the presence of non-Gaussianity in the 21-cm signal, and to quantify one measure of it, we first compare in Figure 2 the probability distribution functions (PDFs) of the 21-cm brightness temperature (Ciardi & Madau 2003; Mellema et al. 2006; Ichikawa et al. 2010) with a Gaussian distribution. At $z = 20$ for each model, we use the variable $\Delta T_{21} = (T_{21} - \bar{T}_{21})$ divided by σ , i.e., the brightness temperature normalized to zero mean (i.e., measured relative to the mean temperature) and unit variance (i.e., divided by the standard deviation of ΔT_{21}). To assess the deviation from a Gaussian distribution, each PDF is compared to a Gaussian distribution, and the difference is also shown for each of the models (in the bottom panel). The standard (CMB only) case, the external radio model, and the radio fluctuation model with the isotropic approximation, all show only a barely noticeable non-Gaussianity in the PDF at this redshift. However, the line of sight effect of bright radio sources, which we have previously shown to enhance the 21-cm power spectrum and its anisotropy (Sikder et al. 2023), also strongly enhances the non-Gaussianity of the 21-cm PDF. Even the moderate case ($f_{\text{Radio}} = 60$) shows a clearly significant deviation from a normal distribution, but the high case ($f_{\text{Radio}} = 3000$) has a highly non-Gaussian PDF; the latter case shows a cutoff on the right-hand side, which corresponds to pixels with no bright radio source behind them (since bright radio sources cause absorption, i.e., a negative 21-cm brightness temperature, and these absorptions are responsible for most of the fluctuations in this case).

In addition to comparing the full PDF with a Gaussian distribution, the non-Gaussianity can be summarized using higher-order moments such as the skewness (a measure of asymmetry) and kurtosis (a measure of the difference between the symmetrically-averaged

distribution and a Gaussian), which are important features of the non-Gaussian PDF of the 21-cm signal (Wyithe & Morales 2007; Harker et al. 2009; Watkinson & Pritchard 2014, 2015; Kubota et al. 2016; Kittiwisit et al. 2017). In Table 2, we list the skewness and kurtosis values at $z = 20$ for the PDFs shown in Figure 2. This quantifies the trends that were qualitatively apparent in Figure 2. During the epoch of the first stars, brightness temperature fluctuations are primarily driven by density and Lyman- α fluctuations, during the time that the spin temperature becomes coupled to the gas temperature through Lyman- α coupling. Since the gas temperature cools more rapidly than the background radiation temperature (which, in the standard astrophysical scenario, is the CMB), the mean spin temperature falls below the background radiation temperature. In the presence of an excess radio background, the contrast between the spin temperature and background radiation temperature increases, depending on the strength of the radio excess relative to the CMB. When the excess radio background originates from early radio galaxies, we find that the skewness becomes negative. However, only the line-of-sight model substantially increases the size of the non-Gaussian moments. For our moderate LoS radio fluctuation model, the skewness increases $\times 8.4$ and the kurtosis $\times 26$ compared to the standard astrophysical scenario, while the high LoS model further increases the skewness $\times 2.5$ and the kurtosis $\times 3.1$. LoS radio fluctuations enhance the absorption in regions surrounding early radio galaxies and along the same line of sight. When the mean number of significant sources is of order one, there are strong Poisson fluctuations and the 21-cm brightness temperature has a highly non-Gaussianity distribution.

With the help of the moments, we can more easily look at the non-Gaussianity as a function of redshift, in order to characterize the properties of each model over a broad range of cosmic history. Figure 3 shows the skewness and kurtosis over a wide redshift range. The non-Gaussianity is in general large towards the end of reionization (large positive skewness and kurtosis, except for the high f_{Radio} case that has a strongly negative skewness) and towards the Dark Ages (negative skewness and positive kurtosis). During cosmic dawn (which is our focus here), the CMB only and external radio cases have nearly identical moments, which are typically of order unity (i.e., not as small as was suggested by the values at $z = 20$). The LoS radio model has significantly larger non-Gaussianity, with a negative skewness and positive kurtosis at all $z \gtrsim 11$. The moderate and high LoS models actually have comparable values of these moments, except that the high model takes off to higher magnitudes at $z \gtrsim 18$. The LoS effect is critical here, as can be seen from the fact that the radio fluctuation model without the LoS effect behaves more similarly to the CMB and external radio models than to the LoS radio models.

The presence of non-Gaussianity in the 21-cm signal indicates that the power spectrum, which can only fully quantify the statistical properties of a Gaussian random field, is insufficient to capture all relevant information. In a purely Gaussian signal, different Fourier modes are independent, meaning that correlations exist only at the two-point level (power spectrum) and all higher-order statistics are zero. However, for the 21-cm signal from cosmic dawn, the bispectrum (three point correlation function) can capture nonlinear and non-Gaussian interactions between different Fourier modes, complementing the power spectrum analysis. Motivated by this, we next investigate how different excess radio models impact the cosmic dawn 21-cm bispectrum.

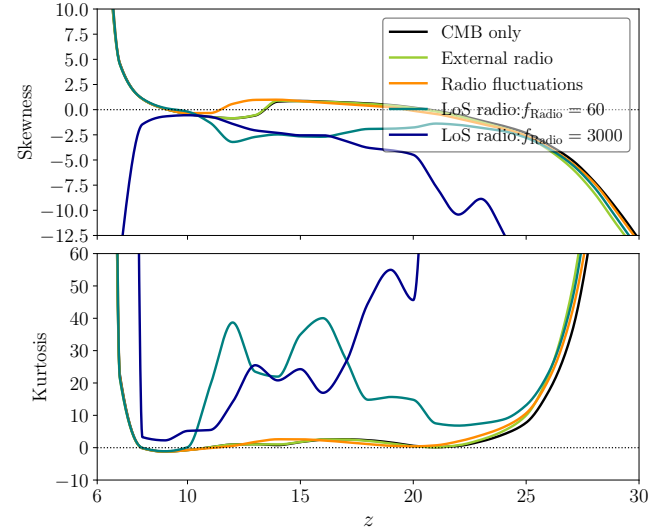


Figure 3. Skewness and kurtosis as a function of redshift, for the same models as shown in Figure 2.

Model	Skewness	Kurtosis
Standard (CMB only)	0.210	0.577
External radio	0.164	0.433
Radio fluctuations	-0.113	0.395
LoS radio: $f_{\text{Radio}} = 60$	-1.771	14.811
LoS radio: $f_{\text{Radio}} = 3000$	-4.484	45.626

Table 2. Skewness and kurtosis at $z = 20$ for our various models considered in this study.

5.2 The effect of an excess radio background on the 21-cm bispectrum

5.2.1 Moderate excess radio backgrounds at redshift 20

With the bispectrum, there is a quite large number of parameters to consider. In order to produce insight rather than confusion, we try to minimize the number of parameters and focus on some regions of the parameter space. As before, we keep the astrophysical model parameters fixed (see Table 1), and consider several distinct excess radio models, alongside the standard astrophysical scenario without any excess radio background (the CMB-only case). We do wish to explore how the various effects vary across cosmic epochs and scales. For simplicity, we begin by only considering in this subsection the radio models with moderate efficiency (i.e., without the high f_{Radio} model), and only at a redshift near the global signal absorption trough for these models, specifically $z = 20$.

Among several simplified triangle configurations, we first consider the case of limiting L-isosceles triangles ($n \rightarrow 1$, i.e., $k_2 \rightarrow k_1$). In Figure 4, we show the SABS for L-isosceles triangles as a function of $\cos \theta$ at three different k_1 values (0.07, 0.244 and 0.851 Mpc^{-1}) for the four different models. The black, green, dark orange, and teal lines indicate the simulation runs without any excess radio background (CMB only), with a uniform external radio background, with isotropic radio fluctuations, and the LoS radio fluctuation model, respectively. In contrast to the power spectrum, the SABS can be positive or negative. We show positive and negative values of the SABS using square and triangle markers, respectively.

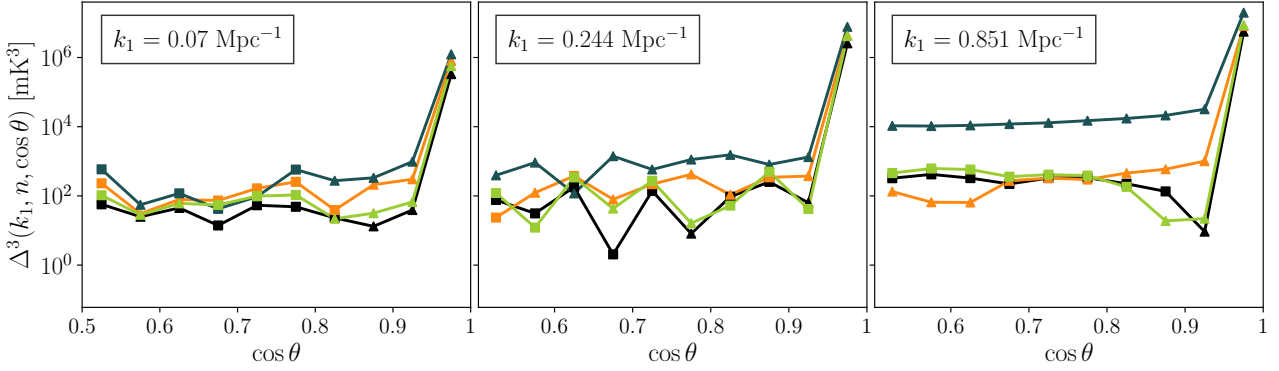


Figure 4. The 21-cm SABS at $z = 20$ for the limiting L-isosceles triangle ($n \rightarrow 1$, i.e., $k_2 \rightarrow k_1$) versus $\cos \theta$ at $k_1 = 0.07, 0.244$ and 0.851 Mpc^{-1} . The square and triangle markers represent positive and negative values of the bispectrum, respectively. The colored lines in each panel show various models: CMB-only (black), external uniform background (green), isotropic (orange) and LoS galactic radio fluctuations (teal).

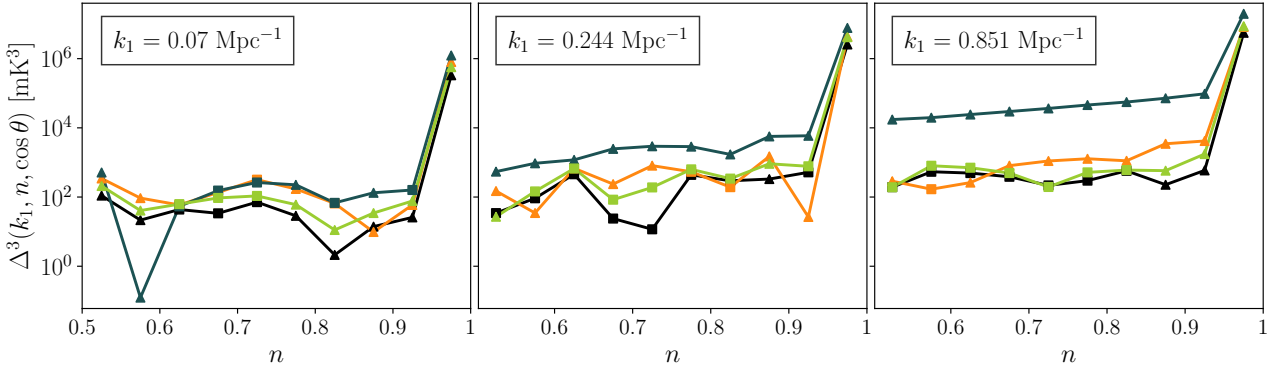


Figure 5. The 21-cm SABS at $z = 20$ for the limiting linear triangles ($\cos \theta \rightarrow 1$) versus n at $k_1 = 0.07, 0.244$ and 0.851 Mpc^{-1} . The markers and colors are as in Figure 4.

The magnitude of the SABS is maximum for all values of k_1 in the $\cos \theta = 0.975$ bin (which is the squeezed limit) and then falls sharply for smaller values of $\cos \theta$. We note that the length of the smallest arm (and hence the area) of the triangles decreases with increasing $\cos \theta$. Now, the squeezed limit ($\cos \theta \rightarrow 1$) corresponds to a triangle configuration where $k_1 \approx k_2 \gg k_3$. This means that the large-scale mode (associated with k_3) modulates the amplitude of small-scale fluctuations. This effect is strongest and most coherent when the modes are aligned ($\cos \theta \rightarrow 1$), leading to the largest amplitude of the SABS. As $\cos \theta$ decreases, the triangle configuration moves away from the squeezed limit towards more equilateral shapes, the strength of the mode coupling weakens, and thus the amplitude of the SABS drops. We also note that for lower values of $\cos \theta$, the SABS values are nearly independent of $\cos \theta$. The flat behavior of the SABS at lower $\cos \theta$ corresponds to triangle configurations where all three wavevectors (k_1, k_2, k_3) are of similar magnitude, resembling near-equilateral triangles. In this regime, the SABS measures the intrinsic non-Gaussianity arising from local, non-linear processes in the 21-cm signal, such as couplings between density and temperature fluctuations, occurring on comparable scales. Unlike the squeezed limit, where a large-scale mode strongly modulates smaller scales, these local interactions are relatively insensitive to the exact triangle shape. As a result, the SABS remains nearly constant across this range of $\cos \theta$, reflecting a consistent level of non-Gaussianity that does not vary much with the angle between the modes.

It is evident that the overall amplitude of the SABS increases

with increasing wavenumber, though random variations occur across different values of $\cos \theta$. On large scales (left and middle panel of Figure 4), the SABS values randomly oscillate between positive and negative in most models. However, on small scales (i.e., larger k_1 , shown in the right panel of Figure 4), the SABS exhibits a distinct bias: it is predominantly positive for the standard astrophysical model (CMB-only case) and the uniform external radio background model, but takes mostly negative values for both galactic radio models. In these models, the spatially varying T_{Radio} (for the isotropic model) or $T_{\text{Radio}, \text{LoS}}$ (for the line-of-sight model) introduces an additional source of fluctuations linked to the density field. By enhancing absorption in overdense regions, T_{Radio} or $T_{\text{Radio}, \text{LoS}}$ amplifies the anti-correlation between density and 21-cm brightness temperature fluctuations. This additional coupling modifies the phase relationships among Fourier modes, resulting in a bispectrum that is biased towards negative values on small scales. Moreover, the LoS effect of radio fluctuations significantly boosts the SABS, increasing its amplitude by approximately two orders of magnitude compared to the standard case for $\cos \theta \leq 0.925$. Thus, on small scales the SABS is particularly sensitive to the LoS radio fluctuations from early radio galaxies. These fluctuations perhaps enhance small-scale non-Gaussianity due to the combination of non-Gaussian Poisson fluctuations, strong anisotropy, and non-linear 21-cm fluctuations.

Next, we present the results for linear triangle configurations ($\cos \theta \rightarrow 1, k_1 \rightarrow k_2 + k_3$). Figure 5 illustrates how the SABS varies with the length of the second largest arm k_2 of triangles, for

the same models and k_1 values as in the previous figure. We vary k_2 by adjusting n for a given k_1 as in Eq. 9. The SABS magnitudes are comparable to those of L-isosceles triangles with the same k_1 values, although there are some random variations between different models. Similarly to the results for limiting L-isosceles triangles, on small scales the LoS effect of radio fluctuations significantly enhances the SABS amplitude by approximately two orders of magnitude compared to the standard astrophysical case and the other two excess radio background models. In the squeezed limit ($n \rightarrow 1$), the SABS amplitudes increase by factors of 3.74, 3.0, and 3.54 relative to the standard astrophysical scenario at $k_1 = 0.07, 0.244$ and 0.851 Mpc^{-1} , respectively. As seen in the L-isosceles triangle results, the SABS values for the LoS radio fluctuation model remain negative across all values of n . These results suggest that the negative SABS values on small scales over the whole range of $\cos \theta$ (limiting L-isosceles triangles) and n (limiting linear triangles) could serve as a potential observational signature of the LoS effect of radio sources from cosmic dawn. We note, though, that these results are based on theoretical simulations, while the practical prospects depend on also accounting for observational errors and artifacts.

In Figure 6 we present the cosmic dawn 21-cm SABS for all unique triangle configurations in the $n - \cos \theta$ space for our four different models at $k_1 = 0.106$ and 0.851 Mpc^{-1} . The figure shows that the SABS is significantly non-zero for almost the entire parameter space of unique triangle configurations, indicating that the 21-cm signal is considerably non-Gaussian during cosmic dawn. In all cases, the SABS amplitude in the squeezed limit configuration (top-right corner of each panel) at $z = 20$ is large and negative. Since the bispectrum for the squeezed limit triangle configuration has the maximum magnitude, this has the highest probability of being detected in upcoming 21-cm experiments (Mondal et al. 2021).

The SABS amplitudes are generally lower in magnitude on large scales ($k_1 = 0.106 \text{ Mpc}^{-1}$) than small scales ($k_1 = 0.851 \text{ Mpc}^{-1}$), across all configurations. The power spectrum is often larger on small scales as well, depending on the dominant source of fluctuations. However, in the SABS the difference is very large, with SABS amplitudes that are orders of magnitude higher on small scales, suggesting that non-Gaussian effects are more pronounced on small scales, particularly when radio fluctuations are present. The LoS radio fluctuation case (right panels) shows the strongest enhancement on small scales, consistent with the idea that small-scale fluctuations are amplified by the Poisson character and strong anisotropy of the galactic radio background.

For the standard astrophysical model (CMB-only case, left panels of Figure 6) and the external radio background model (center-left panel), the SABS is positive for most of the triangle configurations on small scales ($k_1 = 0.851 \text{ Mpc}^{-1}$). In the standard astrophysical model, the Lyman- α fluctuations dominate the 21-cm brightness temperature fluctuations at $z = 20$. These fluctuations drive mode coupling in a way that keeps the SABS positive, particularly at small scales. For equilateral and isosceles triangles, the dominant interaction occurs between modes of similar size. However, in the squeezed limit ($k_1 \approx k_2 \gg k_3$), a large-scale mode (k_3) interacts with two small-scale modes (k_1, k_2). We find a negative SABS in the squeezed-limit case. The external radio model applies a homogeneous excess radio background across all regions; in this model, the dominant fluctuations are still driven by Lyman- α coupling, resulting in a bispectrum that is only mildly altered compared with the CMB-only case.

Unlike the standard and external radio models, which rely mainly on Lyman- α fluctuations to drive the bispectrum, the radio fluctuation models introduce additional structure through spatial variations in the

radio background. If radio fluctuations simply amplified other 21-cm fluctuations uniformly throughout space, the SABS would change at most by an overall scaling. However, in reality, radio fluctuations behave quite differently from Lyman- α fluctuations, and modulate the 21-cm fluctuations in a scale-dependent manner. The result that we find is that the SABS is slightly more negative on large scales, but far more on small scales. The LoS effect introduces additional non-Gaussianity and anisotropy in the 21-cm fluctuations, resulting in a SABS that is even more negative compared to the isotropic radio fluctuation model, especially on small scales.

In order to focus on the effect of the excess radio models, in Figure 7 we show the ratio between the SABS in each excess radio model and the SABS in the standard astrophysical model, throughout the $n - \cos \theta$ space. On large scales (small k_1 , top panel), the typical enhancement of the SABS increases as we go from the external radio model, to the isotropic galactic radio model, to the full LoS galactic radio model; however, no clear pattern emerges in the sign of the SABS ratio, which varies significantly (although it becomes more negative especially for the LoS model). On small scales (large k_1 , bottom panel), the LoS radio model exhibits large ratios, reaching factors of 10 or more, with highly negative values (and positive in a few cases) across many different triangle configurations. In contrast, the external radio model shows relatively small deviations from the standard model, while the isotropic model is intermediate. This again confirms that a uniform radio background does not introduce significant new structure but instead acts as a simple scaling factor. Indeed, the SABS usually does not invert its sign in this case. The SABS in the radio fluctuation models has the opposite sign of the standard model, on this small scale. The LoS radio fluctuations enhance SABS more strongly, leading to higher negative ratios. Since the SABS for the squeezed-limit triangle configuration is negative at cosmic dawn even in the standard case, the SABS ratios for all the excess radio models turn positive in that specific limit. The magnitude and sign of the SABS ratio on small scales across different triangle configurations in the $n - \cos \theta$ space can, in principle, distinguish the type of excess radio background present in the 21-cm signal (i.e., galactic or external), and signify the LoS effect (if present).

5.2.2 More general results

So far in this section, we have examined the impact of moderate excess radio models on the 21-cm SABS at redshift 20, the approximate location of the global signal absorption trough in our four models. In this section, we take a broader look at how excess radio background models affect the 21-cm SABS over the widest redshift range (6 to 30), and compare also to the high galactic radio excess model (with LoS effect).

In Figure 8, we show the evolution of the SABS in the squeezed-triangle limit as a function of redshift, at $k = 0.07, 0.244$ and 0.851 Mpc^{-1} . The inset plot in each panel zooms in to a redshift range corresponding to cosmic dawn. Here, we see several notable features. First, the SABS evolves significantly with redshift, exhibiting notable variations across different cosmic epochs. At early redshifts ($z > 25$), the SABS values are relatively small, as the Lyman- α fluctuations have not yet emerged, and density and temperature fluctuations dominate. During this epoch, the IGM is cold and neutral. As the first sources begin to form, Lyman- α fluctuations from the earliest stars and galaxies become the dominant source of 21-cm fluctuations, resulting in a strong absorption signal. The prominent peak in the SABS that occurs around $z \sim 15 - 25$ (depending on the model) reflects the intense 21-cm absorption due to Lyman- α coupling. This characteristic is qualitatively similar to the power spectrum (illus-

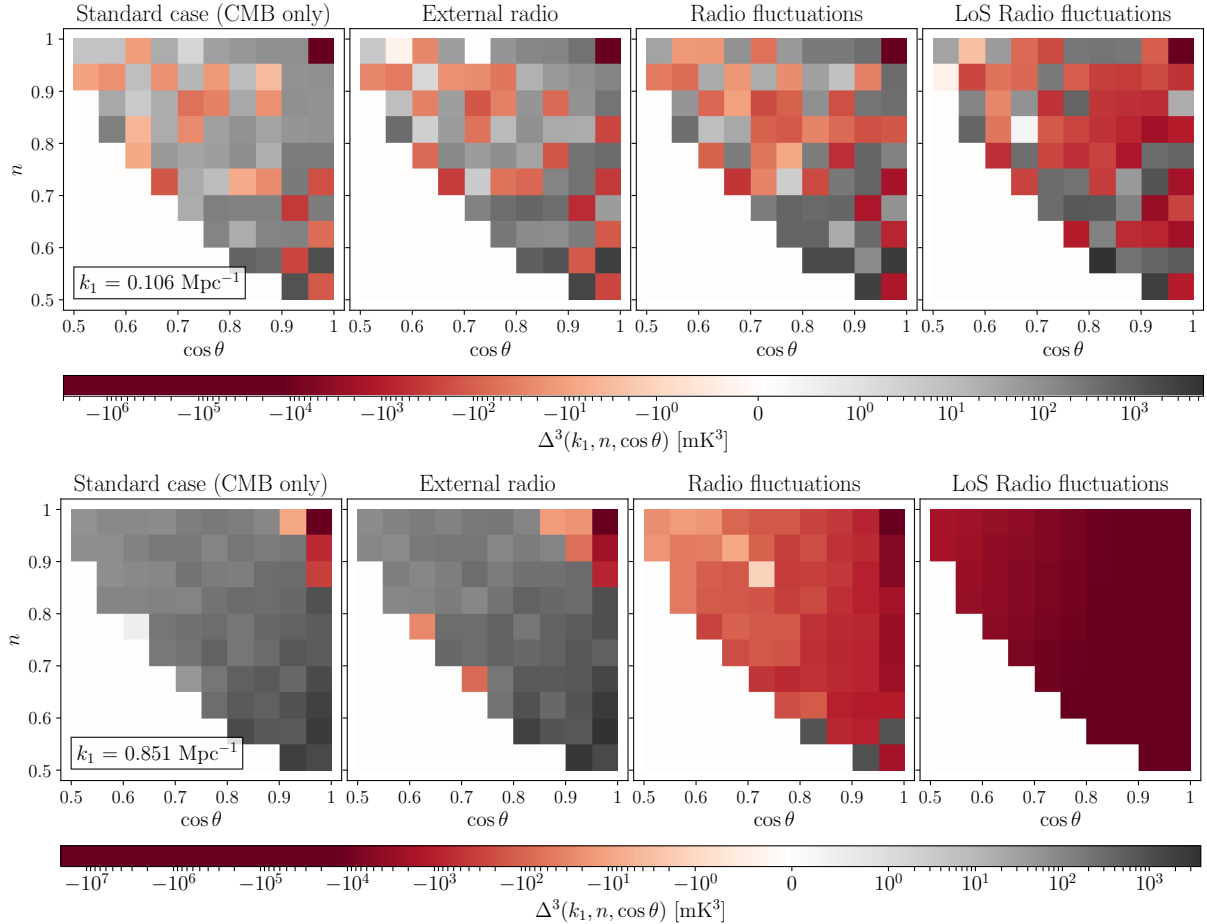


Figure 6. The 21-cm SABS at $z = 20$ for all unique angle configurations for the four models considered in this section: standard astrophysical model (left panel), external radio background (center left), galactic radio background with isotropy (center right) and full galactic radio background with the LoS effect (right), at $k_1 = 0.106$ and 0.851 Mpc^{-1} . The simulations assume the same astrophysical model parameters as discussed in section 2 and presented in Table 1.

trated in the bottom panel of Figure 1). A key feature is that the SABS for the squeezed-limit triangle configuration remains negative throughout the entire cosmic dawn redshift range, in all the models.

At lower redshifts ($z < 15$), the SABS drops, likely due to the onset of the heating transition. As the Universe evolves to lower redshifts, X-ray heating from early galaxies becomes significant, altering the dominant source of 21-cm fluctuations. In regions of high galactic density, the gas is strongly heated, and the spin temperature (T_s) increases, reducing the contrast between T_s and the background radiation temperature. This, in turn, weakens the 21-cm absorption signal. This reduces the correlation between galactic density fluctuations and 21-cm fluctuations. Since the SABS measures how fluctuations at different scales interact, this changes the mode coupling structure observed during the Lyman- α coupling era. In the squeezed limit case, where a long-wavelength mode modulates short-wavelength fluctuations, this new interaction ultimately flips the sign of the SABS from negative to positive as the universe transitions into the heating era. The drop in SABS continues even at even lower redshifts ($z < 10$), as reionization further reduces small-scale fluctuations. However, the high LoS galactic radio model is different from the others; the strong LoS radio fluctuations dominate and produce a very high, and consistently negative, SABS, down to the end of reionization.

As before, the external radio excess only slightly shifts the SABS

amplitudes without altering the overall shape, reinforcing the idea that a uniform background does not change the non-Gaussianities in the signal much. For instance, at $k_1 = 0.244 \text{ Mpc}^{-1}$, the external radio background enhances the SABS by factors of 1.47, 1.55 and 1.76 at $z = 16, 19$ and 22 , respectively. In particular, this boosting factor increases with z , as the spatially uniform external radio background is more intense during early cosmic epochs before cosmic dawn, gradually weakening over cosmic time. In contrast, the excess radio background from early galaxies is non-uniform, and its intensity increases with cosmic time as it traces the formation and growth of galaxies (given our assumption that the radio production efficiency of these galaxies remains constant). For example, at $k_1 = 0.244 \text{ Mpc}^{-1}$, radio fluctuations enhance the SABS (compared to CMB-only) by factors of 10.4, 2.07 and 1.25 at $z = 16, 19$ and 22 , respectively. Since the LoS radio effect introduces additional anisotropy in the 21-cm fluctuations, it further amplifies the SABS. In this case (with a still moderate f_{Radio}), it increases it (compared to CMB-only) by factors of 75.4, 5.27 and 1.52 at $z = 16, 19$ and 22 , respectively. The differences between the isotropic (dark orange) and LoS (teal) radio cases demonstrate that an anisotropic radio background imprints a distinctive non-Gaussian signature on the 21-cm SABS. Finally, the high f_{Radio} LoS model produces a much higher SABS, up to four orders of magnitude higher than even the moderate f_{Radio} LoS model (at $z \sim 10 - 15$).

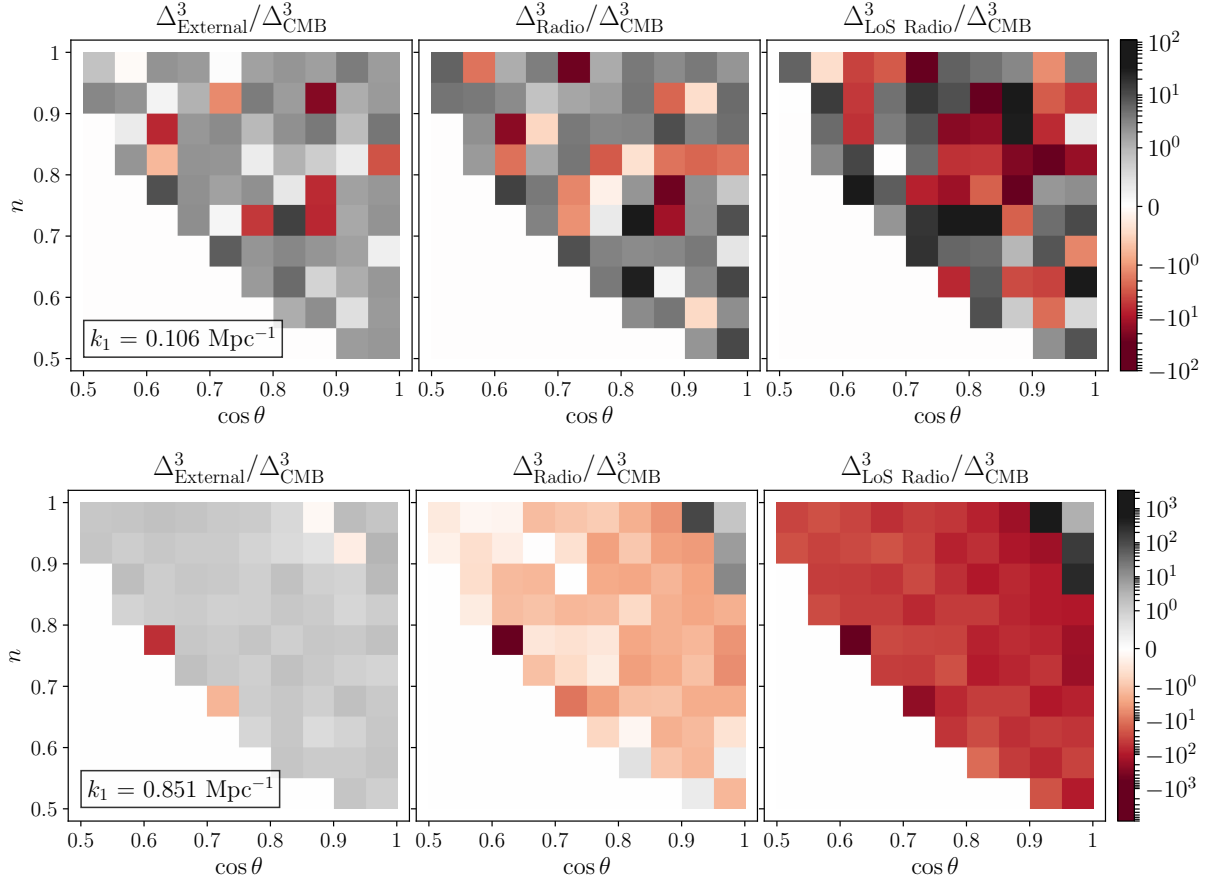


Figure 7. The ratio between the 21-cm SABS at $z = 20$ in excess radio models and that in the standard astrophysical model, shown in the $n - \cos \theta$ space, at $k_1 = 0.106$ and 0.851 Mpc^{-1} . The models shown are: external radio background (left), and galactic radio background with isotropy (center) or with the LoS effect (right).

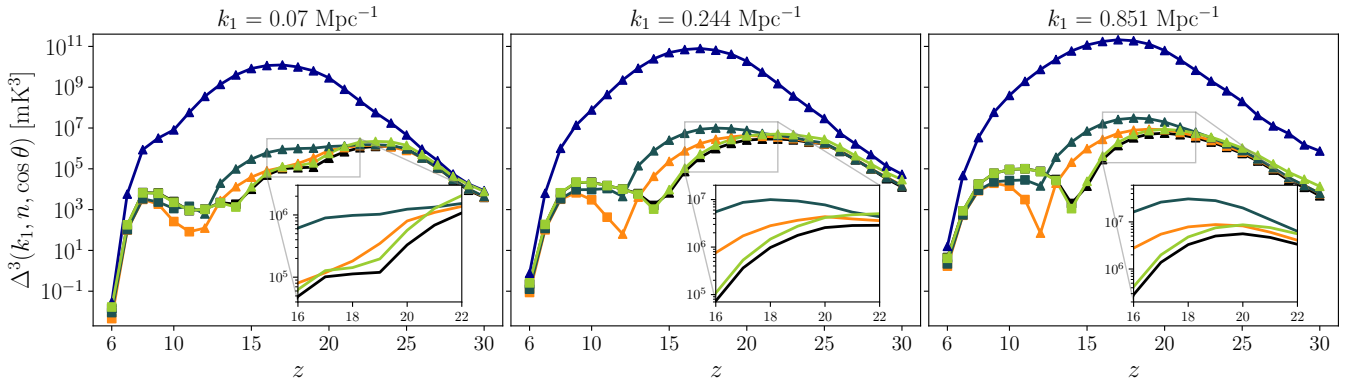


Figure 8. The evolution of the 21-cm SABS as a function of redshift for three different wavenumbers: $k = 0.07$ (left panel), 0.244 (middle panel) and 0.851 Mpc^{-1} (right panel). We show the SABS in the squeezed limit ($\cos \theta \rightarrow 1$, i.e., $k_3 \rightarrow 0$, and $n \rightarrow 1$, i.e., $k_1 \rightarrow k_2$). We show our five models as in Figure 1: the standard astrophysical model (black line), external radio excess (green line), isotropic galactic radio fluctuations (orange line), and LoS galactic radio fluctuation model with $f_{\text{Radio}} = 60$ (teal line) or $f_{\text{Radio}} = 3000$ (blue line). The inset plot in each panel zooms in to a small redshift range showing the differences in SABS values for the standard and moderate radio models. The square and triangle markers represent positive and negative values of the SABS, respectively.

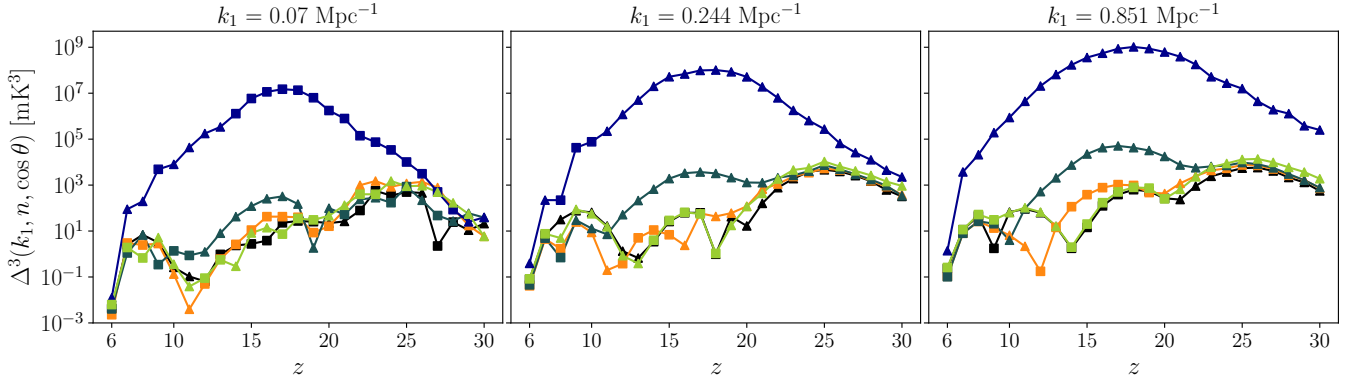


Figure 9. Same as Fig. 8 except that here we show the SABS for $\cos \theta = 0.875$ and $n = 0.875$.

It is important to note the sign change in the squeezed-limit SABS, which reflects a fundamental shift in the dominant physical processes shaping the 21-cm fluctuations. In the CMB-only and external radio background models, the sign transition (from negative to positive) in the squeezed-limit SABS occurs at $z = 14$, marking the beginning of the heating era. However, when an excess galactic radio background over the CMB is present, the coupling transition is delayed because the effective Lyman- α coupling coefficient decreases with the brightness temperature of the radiation background. Furthermore, the heating transition (defined relative to the mean 21-cm background temperature) is also delayed because, in the presence of radio excess, the kinetic temperature needs to reach a higher value, which is the mean $T_{\text{CMB}} + T_{\text{Radio}}$ for the isotropic radio fluctuation model or the mean $T_{\text{CMB}} + T_{\text{Radio, los}}$ for the LoS radio fluctuation model. These mean values are the same (i.e., the LoS model includes the LoS fluctuations of the radio intensity, but the overall mean radio intensity is the same). As a result, in the galactic radio background models, the sign change in the squeezed limit SABS (negative to positive) occurs at a lower redshift compared to the external radio background model and the standard astrophysical model. This delayed heating transition, observed as a sign change at lower redshifts, could serve as a smoking-gun signature of the presence of an excess radio background originating from high-redshift radio-loud sources. This sign-change redshift depends on the strength of the galactic radio background, so that it is $z \sim 11$ for $f_{\text{Radio}} = 60$, while the high $f_{\text{Radio}} = 3000$ pushes it beyond the end of reionization.

During the EoR, the primary driver of 21-cm fluctuations is the formation of ionized bubbles (HII regions) around UV-emitting sources. These bubbles introduce large-scale fluctuations in the 21-cm brightness temperature by creating regions where the signal is suppressed due to ionization. As the number of sources increases, excess radio fluctuations gradually diminish across all scales, causing the power spectrum to converge toward that of the standard astrophysical model. The squeezed-limit SABS follows a similar trend, mirroring the evolution of the power spectrum. Figure 9 shows another example of the evolution of the SABS as a function of redshift, for a triangle configuration that is slightly away from the squeezed limit, with $\cos \theta = 0.875$ and $n = 0.875$, again for $k = 0.07, 0.244$ and 0.851 Mpc^{-1} . The overall behavior of the SABS is similar (as a function of redshift and in terms of the differences among the various models), but the magnitude of the SABS is around two orders of magnitude lower than in the squeezed limit. Also, there are more sign changes so that this feature is more complex to interpret.

Focusing again on the squeezed limit, we show the dependence

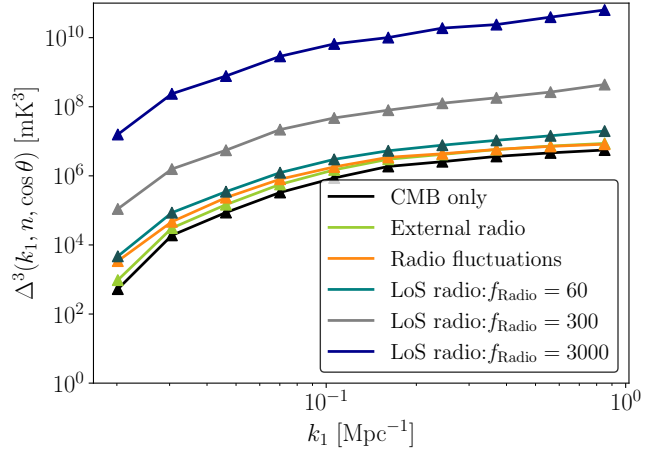


Figure 10. The 21-cm SABS for squeezed-limit triangles ($\cos \theta \rightarrow 1$, i.e., $k_3 \rightarrow 0$, and $n \rightarrow 1$, i.e., $k_1 \rightarrow k_2$) as a function of k_1 at $z = 20$. The triangle markers represent negative values of the bispectrum. The colored lines show various simulation runs: standard astrophysical case (black), external radio (green), isotropic galactic radio (orange) and LoS galactic radio fluctuations (shown for three values of f_{Radio}).

of the SABS at $z = 20$ on k_1 (rather than just a few discrete values of k_1 as in the other figures) in Figure 10. The SABS magnitude increases with k_1 , similarly to the typical behavior of the power spectrum. Since these results correspond to $z = 20$, where Lyman- α -driven fluctuations dominate, all SABS amplitudes are negative. The Lyman- α fluctuations have a natural smoothing, on the typical scale to which the Lyman- α photons travel, and so the increasing curves flatten at high k . However, the LoS fluctuations act over a wide range of scales and reduce this flattening, in addition to their overall boosting of the SABS. For example, at $k_1 = 0.02 \text{ Mpc}^{-1}$, the external, isotropic and LoS radio backgrounds (with $f_{\text{Radio}} = 60$ for the latter two) enhance the squeezed-limit SABS by factors of 1.82, 6.48, and 8.89, respectively, compared to the standard astrophysical model. At $k_1 = 0.85 \text{ Mpc}^{-1}$, these factors are 1.55, 1.47, and 3.54. The effect of an external radio background on the squeezed-limit SABS is fairly scale-independent, as we saw before. In contrast, radio fluctuations have a stronger impact on large scales than on small scales (due to smoothing on the scale of the typical distance to the nearest radio source).

Figure 10 also shows the LoS galactic radio fluctuations for the high $f_{\text{Radio}} = 3000$, and here also for an intermediate case of $f_{\text{Radio}} = 300$ (which, as expected, gives intermediate results for the SABS). Compared to the standard astrophysical case, the squeezed-limit SABS at $k_1 = 0.02 \text{ Mpc}^{-1}$ is enhanced by factors of 209 and 29900 for simulation runs with $f_{\text{Radio}} = 300$ and 3000, respectively. At $k_1 = 0.85 \text{ Mpc}^{-1}$, these factors are 78.5 and 11300. We leave it for future work to analyze the detectability of the cosmic dawn 21-cm SABS in upcoming observations such as those with the SKA-Low.

6 CONCLUSIONS

In this paper, we have presented the effects of excess radio background models on the 21-cm SABS during cosmic dawn. The novelty of this work lies in being the first study to explore the imprint of high-redshift radio fluctuations on the 21-cm SABS during this epoch. We compared three different excess radio background models to the standard astrophysical scenario (CMB-only case), where no excess radio is present. We examined the 21-cm SABS across all unique triangle configurations in the $n - \cos \theta$ space. Since all astrophysical parameters are held fixed, our findings reflect the impact of different excess radio models relative to the standard scenario. The SABS is significantly non-zero across essentially the entire parameter space, confirming that the 21-cm signal is inherently non-Gaussian during cosmic dawn.

In excess radio models, as well as in the standard astrophysical scenario, the value of the squeezed-limit SABS at $z = 20$ is negative. This negative squeezed limit SABS appears to be a characteristic signature of Lyman- α -driven fluctuations. The external radio model introduces a uniform excess radio background, and the mode coupling remains largely similar to that of the standard model. In contrast, radio fluctuations from early galaxies do more than simply amplifying small-scale fluctuations – they impose large-scale structure through spatial variations, modulating their strength in a scale-dependent manner. As a result, the SABS shifts in some cases from positive to negative. The LoS effect introduces additional non-Gaussianity and anisotropy in the 21-cm fluctuations, and often makes the SABS more strongly negative compared to the (artificially) isotropic radio fluctuation model.

Given the inherent complexity of the bispectrum, we simplified the discussion by focusing on the squeezed-limit SABS and its redshift evolution. The SABS evolves significantly with redshift, exhibiting notable variations across different cosmic epochs. The prominent peak in the squeezed limit SABS occurring around $z \sim 15 - 25$ reflects the intense 21-cm absorption due to the underlying Lyman- α coupling. This behavior is similar to that of the power spectrum, except that the squeezed-limit SABS remains negative throughout the entire cosmic dawn redshift range. The sign change in the squeezed-limit SABS marks a fundamental shift in the dominant physical process governing 21-cm fluctuations, and is driven by the heating transition. In the external radio background model, the sign changes at the same redshift as in the standard astrophysical scenario. In the galactic radio background model, the transition from negative to positive squeezed-limit SABS occurs at a lower redshift compared to the standard astrophysical scenario; this redshift is independent of the LoS effect, but depends on the overall efficiency of the galactic radio emission (set by f_{Radio}). We note that the sign is a qualitative feature of the SABS that is not available in the global 21-cm signal or the 21-cm power spectrum.

The amplitude of the squeezed-limit SABS increases with wavenumber (k_1 , corresponding to the largest side of the triangle).

The excess radio background generally enhances the SABS across all scales, with the LoS model exhibiting the strongest amplification. Here we have shown that the 21-cm SABS can in principle provide substantial information on the sources of 21-cm fluctuations. We also considered another signature of non-Gaussianity, namely the probability distribution function of the brightness temperature in 21-cm images. In particular, we considered two higher-order moments, the skewness and kurtosis. The non-Gaussianity is generally large at both low and high redshifts. During cosmic dawn, the LoS model (for moderate or high radio efficiency) is substantially more non-Gaussian by these measures. We leave for future work a detailed analysis of the detectability of these various measures of non-Gaussianity with upcoming radio interferometers.

ACKNOWLEDGEMENTS

SS and RB acknowledge the support of the Israel Science Foundation (grant No. 1078/24). RM is supported by the NITC FRG Seed Grant (NITC/PRJ/PHY/2024-25/FRG/12). RM is grateful for the helpful discussions that Somnath Bharadwaj, Garrelt Mellema, Abinash Kumar Shaw, and Suman Majumdar provided during the development of the Bispectrum estimation code.

This research made use of: Numpy (Harris et al. 2020), Scipy (Virtanen et al. 2020), matplotlib (Hunter 2007) and the NASA Astrophysics Data System Bibliographic Services.

DATA AVAILABILITY

The data underlying this article will be shared on reasonable request to the corresponding author.

REFERENCES

- Abdurashidova Z., et al., 2022a, *ApJ*, **924**, 51
- Abdurashidova Z., et al., 2022b, *ApJ*, **925**, 221
- Acharya S. K., Cyr B., Chluba J., 2023, *MNRAS*, **523**, 1908
- Ali S. S., Bharadwaj S., Chengalur J. N., 2008, *MNRAS*, **385**, 2166
- Barkana R., Loeb A., 2004, *ApJ*, **609**, 474
- Barry N., et al., 2019, *ApJ*, **884**, 1
- Bharadwaj S., Ali S. S., 2005, *MNRAS*, **356**, 1519
- Bharadwaj S., Pandey S. K., 2005, *MNRAS*, **358**, 968
- Bharadwaj S., Mazumdar A., Sarkar D., 2020, *MNRAS*, **493**, 594
- Bowman J. D., Rogers A. E. E., Monsalve R. A., Mozdzen T. J., Mahesh N., 2018, *Nature*, **555**, 67
- Brandenberger R., Cyr B., Shi R., 2019, *J. Cosmology Astropart. Phys.*, 2019, 009
- Ciardi B., Madau P., 2003, *The Astrophysical Journal*, **596**, 1
- Cohen A., Fialkov A., Barkana R., 2016, *MNRAS*, **459**, L90
- Cohen A., Fialkov A., Barkana R., Lotem M., 2017, *MNRAS*, **472**, 1915
- Condon J. J., et al., 2012, *ApJ*, **758**, 23
- Cyr B., Acharya S. K., Chluba J., 2024, *MNRAS*, **534**, 738
- DeBoer D. R., et al., 2017, *PASP*, **129**, 045001
- Dowell J., Taylor G. B., 2018, *ApJ*, **858**, L9
- Ewall-Wice A., Chang T. C., Lazio J., Doré O., Seiffert M., Monsalve R. A., 2018, *ApJ*, **868**, 63
- Feng C., Holder G., 2018, *ApJ*, **858**, L17
- Fialkov A., Barkana R., 2014, *MNRAS*, **445**, 213
- Fialkov A., Barkana R., 2019, *MNRAS*, **486**, 1763
- Fialkov A., Barkana R., Tseliakhovich D., Hirata C. M., 2012, *MNRAS*, **424**, 1335
- Fialkov A., Barkana R., Visbal E., Tseliakhovich D., Hirata C. M., 2013, *MNRAS*, **432**, 2909

Fialkov A., Barkana R., Visbal E., 2014, *Nature*, **506**, 197

Fixsen D. J., et al., 2011, *ApJ*, **734**, 5

Fragos T., et al., 2013, *ApJ*, **764**, 41

Fraser S., et al., 2018, *Physics Letters B*, **785**, 159

Furlanetto S. R., Zaldarriaga M., Hernquist L., 2004, *ApJ*, **613**, 16

Gessey-Jones T., et al., 2022, *MNRAS*, **516**, 841

Ghara R., et al., 2020, *MNRAS*, **493**, 4728

Gilfanov M., Grimm H. J., Sunyaev R., 2004, *MNRAS*, **347**, L57

Grieg B., Mesinger A., 2015, *Monthly Notices of the Royal Astronomical Society*, **449**, 4246

Grieg B., Trott C. M., Barry N., Mutch S. J., Pindor B., Webster R. L., Wyithe J. S. B., 2021, *MNRAS*, **500**, 5322

Grimm H. J., Gilfanov M., Sunyaev R., 2003, *MNRAS*, **339**, 793

Gürkan G., et al., 2018, *MNRAS*, **475**, 3010

Haiman Z., Rees M. J., Loeb A., 1997, *ApJ*, **476**, 458

Harker G. J. A., et al., 2009, *Monthly Notices of the Royal Astronomical Society*, **393**, 1449

Harris C. R., et al., 2020, *Nature*, **585**, 357

Hunter J. D., 2007, *Computing in Science & Engineering*, **9**, 90

Ichikawa K., Barkana R., Iliev I. T., Mellema G., Shapiro P. R., 2010, *Monthly Notices of the Royal Astronomical Society*, **406**, 2521

Iliev I. T., Mellema G., Shapiro P. R., Pen U.-L., 2007, *MNRAS*, **376**, 534

Kamran M., Ghara R., Majumdar S., Mellema G., Bharadwaj S., Pritchard J. R., Mondal R., Iliev I. T., 2022, *J. Cosmology Astropart. Phys.*, **2022**, 001

Kittiwisit P., Bowman J. D., Jacobs D. C., Beardsley A. P., Thyagarajan N., 2017, *Monthly Notices of the Royal Astronomical Society*, **474**, 4487

Koopmans L., et al., 2015, Advancing Astrophysics with the Square Kilometre Array (AASKA14), p. 1

Kubota K., Yoshiura S., Shimabukuro H., Takahashi K., 2016, *Publications of the Astronomical Society of Japan*, **68**, 61

Lewis A., Challinor A., Lasenby A., 2000, *ApJ*, **538**, 473

Li W., et al., 2019, *ApJ*, **887**, 141

Majumdar S., Pritchard J. R., Mondal R., Watkinson C. A., Bharadwaj S., Mellema G., 2018, *MNRAS*, **476**, 4007

Majumdar S., Kamran M., Pritchard J. R., Mondal R., Mazumdar A., Bharadwaj S., Mellema G., 2020, *MNRAS*, **499**, 5090

Mebane R. H., Mirocha J., Furlanetto S. R., 2020, *MNRAS*, **493**, 1217

Mellema G., Iliev I. T., Pen U.-L., Shapiro P. R., 2006, *Monthly Notices of the Royal Astronomical Society*, **372**, 679

Mertens F. G., et al., 2020, *MNRAS*, **493**, 1662

Mineo S., Gilfanov M., Sunyaev R., 2012, *MNRAS*, **419**, 2095

Mirocha J., Furlanetto S. R., 2019, *MNRAS*, **483**, 1980

Mondal R., Bharadwaj S., Majumdar S., Bera A., Acharyya A., 2015, *MNRAS*, **449**, L41

Mondal R., Bharadwaj S., Majumdar S., 2016, *MNRAS*, **456**, 1936

Mondal R., Bharadwaj S., Majumdar S., 2017, *MNRAS*, **464**, 2992

Mondal R., et al., 2020, *MNRAS*, **498**, 4178

Mondal R., Mellema G., Shaw A. K., Kamran M., Majumdar S., 2021, *MNRAS*, **508**, 3848

Pacucci F., Mesinger A., Mineo S., Ferrara A., 2014, *MNRAS*, **443**, 678

Peebles P. J. E., 1980, The large-scale structure of the universe

Planck Collaboration et al., 2016, *A&A*, **594**, A13

Pospelov M., Pradler J., Ruderman J. T., Urbano A., 2018, *Phys. Rev. Lett.*, **121**, 031103

Press W. H., Schechter P., 1974, *ApJ*, **187**, 425

Rees M. J., 1986, *MNRAS*, **222**, 27P

Reis I., Fialkov A., Barkana R., 2020, *MNRAS*, **499**, 5993

Seiffert M., et al., 2011, *ApJ*, **734**, 6

Sheth R. K., Tormen G., 1999, *MNRAS*, **308**, 119

Shimabukuro H., Yoshiura S., Takahashi K., Yokoyama S., Ichiki K., 2015, *Monthly Notices of the Royal Astronomical Society*, **451**, 467

Sikder S., Barkana R., Fialkov A., Reis I., 2023, *Monthly Notices of the Royal Astronomical Society*, **527**, 10975

Sikder S., Barkana R., Fialkov A., 2024, *ApJ*, **970**, L25

Singh S., et al., 2022, *Nature Astronomy*, **6**, 607

Sobacchi E., Mesinger A., 2013, *MNRAS*, **432**, 3340

Subrahmanyan R., Cowsik R., 2013, *The Astrophysical Journal*, **776**, 42

Swarup G., Ananthakrishnan S., Kapahi V. K., Rao A. P., Subrahmanya C. R., Kulkarni V. K., 1991, *Current Science*, Vol. 60, NO.2/JAN25, P. 95, 1991, 60, 95

Tingay S. J., et al., 2013, *Publ. Astron. Soc. Australia*, **30**, 7

Trott C. M., et al., 2020, *MNRAS*, **493**, 4711

Tseliakhovich D., Hirata C., 2010, *Phys. Rev. D*, **82**, 083520

Tseliakhovich D., Barkana R., Hirata C. M., 2011, *MNRAS*, **418**, 906

Virtanen P., et al., 2020, *Nature Methods*, **17**, 261

Visbal E., Barkana R., Fialkov A., Tseliakhovich D., Hirata C. M., 2012, *Nature*, **487**, 70

Watkinson C. A., Pritchard J. R., 2014, *Monthly Notices of the Royal Astronomical Society*, **443**, 3090

Watkinson C. A., Pritchard J. R., 2015, *Monthly Notices of the Royal Astronomical Society*, **454**, 1416

Watkinson C. A., Majumdar S., Pritchard J. R., Mondal R., 2017, *MNRAS*, **472**, 2436

Wyithe J. S. B., Morales M. F., 2007, *Monthly Notices of the Royal Astronomical Society*, **379**, 1647

van Haarlem M. P., et al., 2013, *A&A*, **556**, A2

This paper has been typeset from a *TeX/LaTeX* file prepared by the author.